Title	Interfacial Electron Flow Control by Double Nano-architectures for Efficient Ru-Dye-Sensitized Hydrogen Evolution from Water
Author(s)	Yoshimura, Nobutaka; Kobayashi, Atsushi; Kondo, Tomoki; Abe, Ryu; Yoshida, Masaki; Kato, Masako
Citation	ACS applied energy materials, 4(12), 14352-14362 https://doi.org/10.1021/acsaem.1c03028
Issue Date	2021-12-27
Doc URL	http://hdl.handle.net/2115/87655
Rights	This document is the Accepted Manuscript version of a Published Work that appeared in final form in ACS applied energy materials, copyright c American Chemical Society after peer review and technical editing by the publisher. To access the final edited and published work see https://pubs.acs.org/articlesonrequest/AOR-PPA5PRNCZZT62THU9ZZI.
Type	article (author version)
File Information	ACS Appl. Energ. Mater._4(12)_14352-14362.pdf

Interfacial Electron Flow Control by Double Nano-architectures for Efficient Ru-dye-sensitized Hydrogen Evolution from Water

Nobutaka Yoshimura,[#] Atsushi Kobayashi,*[#] Tomoki Kondo,[§] Ryu Abe,[§] Masaki Yoshida,[#] Masako Kato[#†].

[#]Department of Chemistry, Faculty of Science, Hokkaido University, North-10 West-8, Kita-ku, Sapporo 060-0810, Japan.

[§]Department of Energy and Hydrocarbon Chemistry, Graduate School of Engineering, Kyoto University, Nishikyo-ku, Kyoto 615-8510, Japan.

ABSTRACT: Interfacial electron flow is crucial for efficient two-step (Z-scheme) solar water splitting reaction. Dye-sensitization of a wide-gap oxide semiconductor has attracted considerable attention for decades as a means of producing hydrogen from water; however, it suffers from back electron transfer reactions at solid-solid and solid-solution interfaces. Here, we demonstrate that combination of two nano-architectures, Ru-dye double-layering and Pt-cocatalyst intercalation to layered niobate semiconductor, effectively suppresses the back electron transfers at interfaces, leading to the complete oxidation of [Co(bpy)₃]-type electron mediator (bpy = 2,2′-bipyridine) as a result of efficient photocatalytic hydrogen production. Our systematic study on the Ru-dye double layers revealed that the double layering of two different Ru dyes and surface modification with Zr^{4+} cation not only suppresses the back electron transfer from electron-injected semiconductor to oxidized dye, but also accelerates the electron injection from the mediator to oxidized dye. In addition, the re-reduction of oxidized Co(III) mediator at the Pt cocatalyst surface was effectively suppressed by intercalation to the layered niobate semiconductor. The present work clearly shows that double nano-architectures controlling the surfaces of semiconductor and cocatalyst have great potential for photo-induced charge-separation at the solid-solution interface and expands the possibilities of layered semiconductor materials toward Z-scheme water splitting.

INTRODUCTION

The photocatalytic solar water-splitting reaction has recently attracted considerable attention as a promising approach to solve global warming and energy resource issues (1–5). Since the discovery of the Honda–Fujishima effect (6), many semiconductor photocatalysts have been developed (1,7–15). Recently, K. Domen *et al.* achieved 96% apparent quantum yield (AQY) at 360 nm UV light excitation for Al-doped $SrTiO_3$, in which the two different cocatalysts were loaded on the different crystal facets (16). This technique, which is based on the two different crystal facets, is remarkably effective for charge separation in a bulk semiconductor photocatalyst (17,18). However, the achievement of 100% AQY for visible-light-driven water splitting remains challenging. Two-step photocatalytic water splitting (Z-scheme) systems coupled with a suitable electron mediator have been extensively studied to utilize visible light in the solar spectrum, because of the wide tunability of both their light absorption and redox potentials (19–22). In such a Z-scheme photocatalysis process, one-way electron transfer from the oxygen- to the hydrogen-evolving photocatalyst is strongly required. In this context, various electron mediators ranging from soluble molecular mediators, such as I_3^-/I^- and $[Co(bpy)_3]^{3+/2+}$ (bpy = 2,2′-bipyridine), to solid mediators like a photoreduced graphene oxide, have been developed (23–25). However, back electron transfer at the photocatalyst–mediator interface remains a bottleneck issue.

Dye-sensitization based on photoinduced interfacial electron injection from a surface-immobilized photosensitizer (PS) to a semiconductor substrate is another promising method to utilize visible light for water splitting (26–38). The typical n-type semiconductor TiO_2 has been widely used as a substrate to fabricate H_2 evolution dye-sensitized photocatalysts (DSPs). In addition, several noteworthy works have suggested that layered metal oxides are also promising candidates for the fabrication of highly active DSPs (39–41). For example, Mallouk *et al.* reported a DSP composed of the Pt-cocatalyst-loaded layered niobate $Pt/K_{4-x}H_xNb_6O_{17}$ and a carboxy-functionalized Ru(II) PS (42,43). This DSP is active for H_2 evolution reaction, even in an iodide aqueous solution that can act as an electron mediator. Abe *et al.* achieved overall water splitting using the coumarin-dye-sensitized internally platinated layered niobate $Pt/H_4Nb_6O_{17}$ as the H_2 evolution DSP and IrO_2-cocatalyst-loaded WO_3 as the O_2 evolution photocatalyst in the presence of an iodide mediator (I_3^-/I^-) (44). Further progress was recently reported by Maeda *et al.*, in that the surface deposition of Al_2O_3 clusters on an Ru(II)-dye-sensitized $Pt/HCa_2Nb_3O_{10}$ photocatalyst is effective for charge separation at the semiconductor–mediator interface

Scheme 1. Schematic surface structures of three types of PS-double-layered Pt/$K_xH_{4-x}Nb_6O_{17}$ photocatalysts: (a) Zr-**RuCP⁶**-Zr-**RuP⁶**@Pt/$K_xH_{4-x}Nb_6O_{17}$, (b) **RuCP⁶**-Zr-**RuP⁶**@Pt/$K_xH_{4-x}Nb_6O_{17}$, and (c) **RuCP²**-Zr-**RuP⁶**@Pt/$K_xH_{4-x}Nb_6O_{17}$.
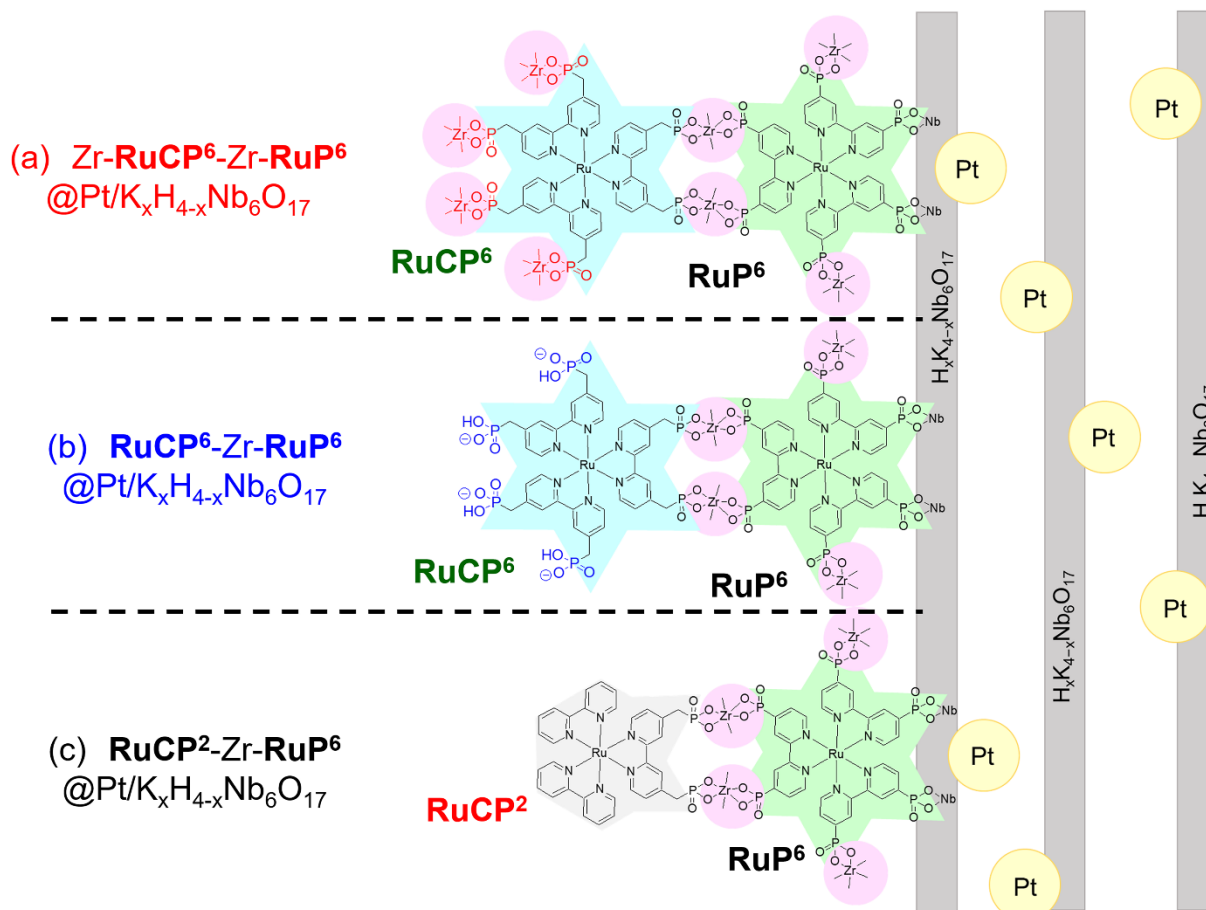
(AQY = 2.4% at 420 nm) (45). These pioneering works indicate the importance of the surface structure of a DSP, but further investigation of the interfacial structure between the layered metal oxide semiconductor surface and solution mediator is strongly required.

In this work, we newly fabricated a DSP system by using two different nano-architectures, Ru-dye double layering and Pt co-catalyst intercalation, to overcome the back reactions at the solid–solution interface. The DSP reported herein is composed of the internally platinated layered niobate Pt/$K_xH_{4-x}Nb_6O_{17}$ sensitized by double-layered Ru(II) dyes with different surface functional groups: **RuCP²**-Zr-**RuP⁶**@Pt/$K_xH_{4-x}Nb_6O_{17}$, **RuCP⁶**-Zr-**RuP⁶**@Pt/$K_xH_{4-x}Nb_6O_{17}$, and Zr-**RuCP⁶**-Zr-**RuP⁶**@Pt/$K_xH_{4-x}Nb_6O_{17}$ {Scheme 1; **RuCP²** = [Ru(bpy)₂(mpbpy)]²⁻, **RuCP⁶** = [Ru(mpbpy)₃]¹⁰⁻, **RuP⁶** = [Ru(pbpy)₃]¹⁰⁻, bpy = 2,2′-bipyridine, H₄mpbpy = 2,2′-bipyridine-4,4′-bis(methane-phosphonic acid), and H₄pbpy = 2,2′-bipyridine-4,4′-bis(phosphonic acid)}. This strategy not only effectively suppresses the back reaction of the internally loaded Pt cocatalysts, as previously reported, (44) but also enabled us to control the reactivity with the electron mediators based on the surface structure and thus, the immobilized PS molecules (46–48). We demonstrate that the double layering of Ru(II) PS remarkably improved the photocatalytic H₂ evolution activity (AQY ~0.4% at 470 nm) in redox-reversible electron donors (iodide or

[Co(bpy)₃]²⁺) and that the surface functional groups significantly affected the reactivity with these electron sources. Notably, **RuCP⁶**-Zr-**RuP⁶**@Pt/$K_xH_{4-x}Nb_6O_{17}$ continued to evolve H₂ until all the [Co(bpy)₃]²⁺ donor species were consumed, even in the presence of an equimolar amount of the oxidized Co(III) mediator [Co(bpy)₃]³⁺. These results indicate that dye assembly at the solid–solution interface coupled with the intercalation of cocatalyst to the layered semiconductor is a promising approach to achieve one-way electron transfer in Z-scheme water splitting photocatalysts.

RESULTS AND DISCUSSION

Single-layered Ru(II)-dye-immobilized Pt/$K_xH_{4-x}Nb_6O_{17}$

Figure 1 summarizes the estimated amount of Ru(II)-dye molecules immobilized onto the surface of 1 mg particulate Pt/$K_xH_{4-x}Nb_6O_{17}$ sample. This was estimated from the decreased amount of dye molecules in the supernatant solutions, determined by comparing the UV-vis spectra before and after the immobilization process (see ESI, Figure S1 and, Table S1). For the PS single layers (**RuCP²** and **RuP⁶**), the amount of **RuCP²** dye immobilized on Pt/$K_xH_{4-x}Nb_6O_{17}$ was approximately double that of the **RuP⁶** dye, probably owing to the difference in the occupied area of each dye molecule. **RuP⁶** possesses more (six)

phosphonate moieties than **RuCP²** (two), and thus, compared to **RuCP²**, it sterically and electrostatically occupies a larger area of the $Pt/K_xH_{4-x}Nb_6O_{17}$ surface. This results in a smaller amount of **RuP⁶** being immobilized. A similar trend was previously reported for $Pt-TiO_2$ (48). The validity of the estimated values (e.g., 54 nmol/g for **RuP⁶**) was assessed by considering the surface area of the $Pt/K_xH_{4-x}Nb_6O_{17}$ particles. The thickness of a $Pt/K_xH_{4-x}Nb_6O_{17}$ platelet particle was estimated to be 11 ± 1 nm, based on the full width at half maximum of the (040) reflection of the PXRD pattern (Figure S2), while the average length and/or width, determined from the TEM images, was in the range 20–200 nm (Figure S3). Assuming the shape of a $Pt/K_xH_{4-x}Nb_6O_{17}$ particle as rectangular parallelepiped, the immobilization amount per unit area of $Pt/K_xH_{4-x}Nb_6O_{17}$ is 0.018–0.121 $nmol/cm^2$ (see "Calculation of the surface coverage of Ru(II) complexes per unit area of $K_xH_{4-x}Nb_6O_{17}$" in the supporting information). This value approaches the calculated value ($\sim$0.083 $nmol/cm^2$) based on the occupied area of one **RuP⁶** molecule ($\sim$2 nm^2 per one molecule), strongly suggesting that the surfaces of a $Pt/K_xH_{4-x}Nb_6O_{17}$ particle are almost fully covered by **RuP⁶**. This hypothesis was supported by the fact that no significant adsorption occurred in the subsequent (second) **RuP⁶** immobilization reaction without Zr(IV) cation linkers. Indeed, the UV-vis absorption spectra of the supernatant solution was near-identical to that recorded before the reaction (Figure S4). In addition, no characteristic **RuP⁶** absorption band was observed for the supernatant solution obtained after subsequent reaction with the Zr^{4+} cation to prepare the Zr-**RuP⁶**@$Pt/K_xH_{4-x}Nb_6O_{17}$ precursor (Figures S1c and S1f) for double layer formation.

Double-layered Ru(II)-dye-immobilized $Pt/K_xH_{4-x}Nb_6O_{17}$

As seen in Figure 1, all three samples with PS-double-layered Ru dyes prepared using the Zr(IV) cation linkers were confirmed to contain at least double the amount of immobilized dye molecules than that of the single-layered sample (**RuP⁶**@$Pt/K_xH_{4-x}Nb_6O_{17}$). Moreover, the negligible desorption of **RuP⁶** during the subsequent reaction with the Zr^{4+} cation indicates that the immobilized amount of **RuP⁶** dye in Zr-**RuP⁶**@$Pt/K_xH_{4-x}Nb_6O_{17}$ is near-identical to that of **RuP⁶**@$Pt/K_xH_{4-x}Nb_6O_{17}$. Notably, neither desorption of **RuP⁶** nor dye exchange from **RuP⁶** to the dye used for the second layer (e.g., **RuCP²** or **RuCP⁶**) occurred, as confirmed by the emission and ^{1}H NMR spectra and emission decay curve of the supernatant solution isolated from the second dye immobilization reaction (Figure S5). All three results were near-identical to that of the **RuCP⁶** dye aqueous solution, and no signals assignable to **RuP⁶** were detected. As was observed for the single-layered sample, the amount ($\sim$92 nmol) of immobilized **RuCP²** in **RuCP²**-Zr-**RuP⁶**@$Pt/K_xH_{4-x}Nb_6O_{17}$ was 35% larger than that ($\sim$69 nmol) of **RuCP⁶** in **RuCP⁶**-Zr-**RuP⁶**@$Pt/K_xH_{4-x}Nb_6O_{17}$. This was attributed to the smaller size and neutral nature of **RuCP²**. In the **RuCP²**-Zr-**RuP⁶**@$Pt/K_xH_{4-x}Nb_6O_{17}$ sample, the amount of outer **RuCP²** was approximately 1.3 times larger than that of the inner **RuP⁶**. This seems quite reasonable on considering the number of phosphonic acid groups in each dye: The **RuP⁶** dye in the inner layer is immobilized on the surface of $K_xH_{4-x}Nb_6O_{17}$ by three phosphonate linkers, leaving three free phosphonates for binding to the Zr^{4+} cations. If the **RuCP²**, with two phosphonates, occupies two of the three surface-bound Zr^{4+} sites to form the second outer layer, the maximum amount of immobilized **RuCP²** will

be approximately one and a half times the amount of **RuP⁶** in the inner layer, reasonably explaining the above result.
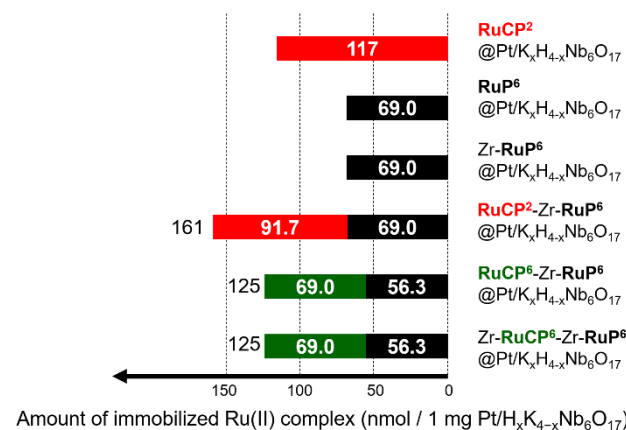

Figure 1. Amounts of immobilized Ru(II) complexes on $Pt/K_xH_{4-x}Nb_6O_{17}$. Two different batches of **RuP⁶**@$Pt/K_xH_{4-x}Nb_6O_{17}$ were used for Zr-**RuP⁶**@$Pt/K_xH_{4-x}Nb_6O_{17}$, **RuCP²**-Zr-**RuP⁶**@$Pt/K_xH_{4-x}Nb_6O_{17}$ and **RuCP⁶**-Zr-**RuP⁶**@$Pt/K_xH_{4-x}Nb_6O_{17}$, Zr-**RuCP⁶**-Zr-**RuP⁶**@$Pt/K_xH_{4-x}Nb_6O_{17}$, with immobilized **RuP⁶** dye concentrations of 69.0 nmol/mg and 56.3 nmol/mg, respectively.

This is also a reasonable explanation for the comparable immobilization amounts of the two Ru(II) dyes in **RuCP⁶**-Zr-**RuP⁶**@$Pt/K_xH_{4-x}Nb_6O_{17}$. This is because **RuCP⁶**, with six phosphonates, can occupy all the three surface-bound Zr^{4+} sites, resulting in the 1:1 molar ratio of these two Ru(II) dyes. As discussed above, no [1]MLCT absorption band derived from the Ru(II) dyes was detected in the UV-vis absorption spectrum of the supernatant solution obtained after the Zr^{4+} immobilization reaction to form Zr-**RuCP⁶**-Zr-**RuP⁶**@$Pt/K_xH_{4-x}Nb_6O_{17}$ (Figure S1f). Thus, we concluded that the immobilization amount of each Ru(II) dye in Zr-**RuCP⁶**-Zr-**RuP⁶**@$Pt/K_xH_{4-x}Nb_6O_{17}$ is near-identical to that in **RuCP⁶**-Zr-**RuP⁶**@$Pt/K_xH_{4-x}Nb_6O_{17}$.

The chemical composition of each sample was estimated by XRF (Figure S6). We confirmed that the unmodified $Pt/K_xH_{4-x}Nb_6O_{17}$ sample only exhibited peaks derived from Pt and Nb. On the other hand, all the Ru(II)-dye-immobilized $Pt/K_xH_{4-x}Nb_6O_{17}$ particles exhibited Ru $K\alpha$ radiation at 19.2 keV, confirming the presence of immobilized Ru(II) dyes on the surface. Although quantitative analysis on the amount of each Ru(II) dye was difficult, owing to the overlap between the Ru $K\alpha$ and Nb $K\beta$ radiations, the Ru $K\alpha$ intensity of the PS-double-layered $Pt/K_xH_{4-x}Nb_6O_{17}$ was significantly stronger than that of the PS-single-layered counterpart. All the Zr^{4+}-treated samples, namely Zr-**RuP⁶**@$Pt/K_xH_{4-x}Nb_6O_{17}$, **RuCP²**-Zr-**RuP⁶**@$Pt/K_xH_{4-x}Nb_6O_{17}$, and **RuCP⁶**-Zr-**RuP⁶**@$Pt/K_xH_{4-x}Nb_6O_{17}$ presented a Zr $K\alpha$ peak at 15.7 keV, confirming that the Zr^{4+} cations were bound by the phosphonates of the Ru(II) dyes. As expected, the Zr $K\alpha$ peak intensity of Zr-**RuCP⁶**-Zr-**RuP⁶**@$Pt/K_xH_{4-x}Nb_6O_{17}$ was larger than that of **RuCP⁶**-Zr-**RuP⁶**@$Pt/K_xH_{4-x}Nb_6O_{17}$, indicating an increased amount of Zr^{4+} cations as a result of their immobilization to the phosphonate groups directed on the outside of the **RuCP⁶** layer. PXRD measurements revealed that the effect of Ru(II)-dye-immobilization on the crystal structure of the $Pt/K_xH_{4-x}Nb_6O_{17}$ particles was negligible (Figure S2).

Photocatalytic H₂ evolution reaction using KI as anionic electron donor

Figure 2 shows the time courses of photocatalytic hydrogen evolution on the Ru(II)-dye-immobilized Pt/$K_xH_{4-x}Nb_6O_{17}$ samples from aqueous KI solution (0.5 M, pH = 2), in which the iodide anions act as electron donors. In addition, the TON, TOF, and AQY values estimated for each reaction are summarized in Table 1. Note that the total amount of Ru(II) dye in each solution was constant (100 μM) and no hydrogen evolution was observed in the absence of Ru(II) PS, light, or electron donor (Table S2). As seen in Figure 2, all six samples, including the PS-single-layered samples, evolved H₂ with relatively steady rates. This is in stark contrast to previously reported results with Pt-TiO₂ nanoparticles, in which the PS-single-layered Pt-TiO₂ nanoparticles did not show any reliable H₂ production under the same conditions (47). This implies the crucial role of the Pt co-catalyst loaded in the interlayer of $K_xH_{4-x}Nb_6O_{17}$, as discussed in various literature (41–45). As seen in Table 1, all six samples

exhibited TONs >1, confirming the occurrence of H₂ production via photocatalytic processes triggered by light absorption of a Ru(II) PS and subsequent electron donation from the iodide as the electron source. Clearly, the PS-double-layered particles evolved two- to fourfold the amount of H₂ than did the PS-single-layered particles with the same surface functional (Zr-PO₃-, PO₃-, or H-) group. This was attributed to the improved charge separation between the semiconductor and Ru(II) dyes, as we previously reported for the Pt-TiO₂ nanoparticles (49). Briefly, the back electron transfer can be suppressed by the introduction of PS-dye-double-layered particles. This suppression can be explained by the energy diagram shown in Scheme 2, which reveals that hole transfer from the inner to the outer PS is possible. These results suggest that PS-multilayering is a promising method to improve the charge-separation efficiency not only for the classical TiO₂ but also for the layered niobate $K_xH_{4-x}Nb_6O_{17}$. More interestingly, the activity of the PS-double-layered particles strongly depended on the surface functional group.
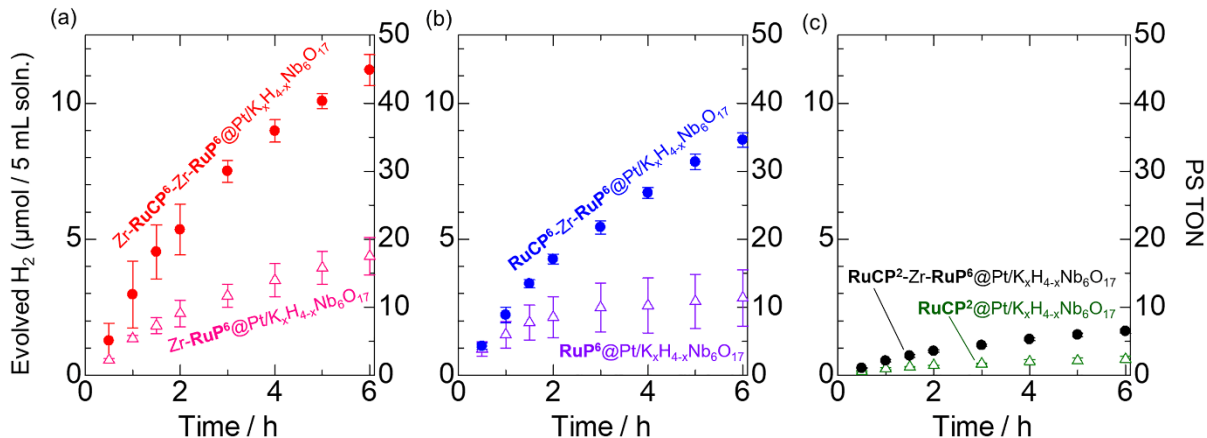

Figure 2. Photocatalytic H₂ evolution reactions driven by (a) Zr-**RuCP⁶**-Zr-**RuP⁶**@Pt/$K_xH_{4-x}Nb_6O_{17}$ (red closed circles) and Zr-**RuP⁶**@Pt/$K_xH_{4-x}Nb_6O_{17}$ (pink open triangles), (b) **RuCP⁶**-Zr-**RuP⁶**@Pt/$K_xH_{4-x}Nb_6O_{17}$ (blue closed triangles) and **RuP⁶**@Pt/$K_xH_{4-x}Nb_6O_{17}$ (purple open triangles), and (c) **RuCP²**-Zr-**RuP⁶**@Pt/$K_xH_{4-x}Nb_6O_{17}$ (black closed circles) and **RuCP²**@Pt/$K_xH_{4-x}Nb_6O_{17}$ (green open circles) in the presence of 100 μM Ru(II) dye and 0.5 M KI as the electron donor (initial pH = 2.0, λ = 470 ± 10 nm).

Table 1. Results of photocatalytic H₂ evolution experiments in 0.5 M KI aqueous solution.

Photocatalyst[a]	H₂ (μmol) (0–6 h)	Produced I_3^- (μmol)	PS TON[a] (0–3 h)	PS TON[a] (0–6 h)	PS initial TOF[a]	AQY[a] (%) (0–6 h)	iAQY[a] (%) (0–1 h)
RuCP²@Pt/$K_xH_{4-x}Nb_6O_{17}$	0.589±0.114	0.33	1.58	2.36	1.0	0.020	0.049
RuP⁶@Pt/$K_xH_{4-x}Nb_6O_{17}$	2.84±1.04	3.0	9.96	11.4	6.0	0.10	0.30
Zr-**RuP⁶**@Pt/$K_xH_{4-x}Nb_6O_{17}$	4.38±0.68	3.7	11.6	17.5	5.4	0.15	0.27
RuCP²-Zr-**RuP⁶**@Pt/$K_xH_{4-x}Nb_6O_{17}$	1.62±0.08	1.5	4.40	6.48	2.1	0.054	0.11
RuCP⁶-Zr-**RuP⁶**@Pt/$K_xH_{4-x}Nb_6O_{17}$	8.64±0.26	7.7	21.8	34.6	8.9	0.29	0.45
Zr-**RuCP⁶**-Zr-**RuP⁶**@Pt/$K_xH_{4-x}Nb_6O_{17}$	11.2±0.56	9.2	30.0	44.9	7.9	0.38	0.60

[a]Reaction conditions: [Ru-PS] = 100 μM in total, [KI] = 0.5 M, HCl aqueous solution (pH = 2), $λ_{ex}$ = 470 ± 10 nm, 70 mW. The reaction solution was purged by Ar bubbling for 1 h before light irradiation. The numerical values are averages of more than three experiments. Definitions: TON, turn-over number; TOF, turn-over frequency; AQY, apparent quantum yield. Average value of produced H₂ was used in these calculations.

Scheme 2. Energy diagram of Ru(II)-PS double-layered Pt/$K_xH_{4-x}Nb_6O_{17}$ photocatalytic system in aqueous solution
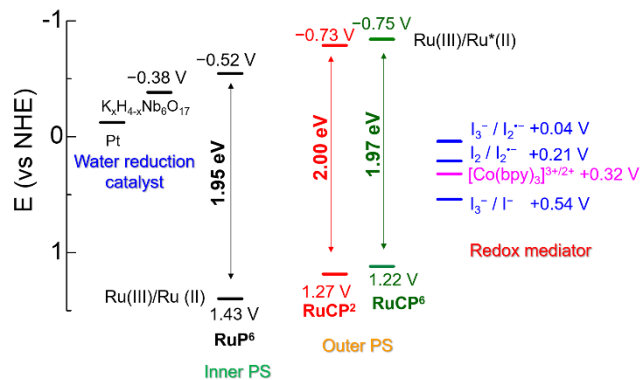
After 6 h irradiation, the TONs of **RuCP^6**-Zr-**RuP^6**@Pt/$K_xH_{4-x}Nb_6O_{17}$ and Zr-**RuCP^6**-Zr-**RuP^6**@Pt/$K_xH_{4-x}Nb_6O_{17}$ were respectively approximately five and seven times higher than that of **RuCP^2**-Zr-**RuP^6**@Pt/$K_xH_{4-x}Nb_6O_{17}$. The Ru(III)/Ru(II) redox potentials of **RuCP^2** and **RuCP^6** immobilized in the second outer layer were reported to be near-identical by Meyer *et al.* (49) (Scheme 2). In addition, coordination to Zr^{4+} had little effect on these values. Thus, the difference in activity was not thermodynamically (redox potential) induced but originated from the geometrical difference in the outer surface structure, as reported in the previously reported Pt-TiO_2 nanoparticle system (48). Hence, iodide anions are attracted by the electrostatic and/or hydrogen bonding interactions with the surface functional groups of Zr-**RuCP^6**-Zr-**RuP^6**@Pt/$K_xH_{4-x}Nb_6O_{17}$ and **RuCP^6**-Zr-**RuP^6**@Pt/$K_xH_{4-x}Nb_6O_{17}$, enabling more efficient electron injection to the photo-oxidized Ru(III) dye. In the present Zr-**RuCP^6**-Zr-**RuP^6**@Pt/$K_xH_{4-x}Nb_6O_{17}$, the iodide anions are attracted by the Zr^{4+}-phosphonate groups at the outer surface, whereas they are electrostatically repelled by the surface phosphonate groups of **RuCP^6**-Zr-**RuP^6**@Pt/$K_xH_{4-x}Nb_6O_{17}$. The zeta potential of Zr-**RuCP^6**-Zr-**RuP^6**@Pt/$K_xH_{4-x}Nb_6O_{17}$ in the absence of iodide aqueous solution was positive, assumptions are supported by the zeta potential measurements while a large negative shift was observed following the addition of 0.5 M iodide (Table S3, +31 mV → +4.9 mV), suggesting the attraction of iodide anions to the particle surface. These results are consistent with those from the recent work on a dye-sensitized solar cell by Hanson *et al.*, whereby the surface Zr^{4+}-phosphonate moiety attached on a well-known Ru(II) dye (N3) suppressed back electron transfer from the redox mediator to improve the open circuit voltage (V_{OC}) (50). On the other hand, the change in the zeta potential of **RuCP^6**-Zr-**RuP^6**@Pt/$K_xH_{4-x}Nb_6O_{17}$ was negligible when iodide was added (+2.9 mV → +1.0 mV). Given that the pKa of phosphonic acid is ~1.5 (51), the particle surface of **RuCP^6**-Zr-**RuP^6**@Pt/$K_xH_{4-x}Nb_6O_{17}$ can be neutralized by the proton release from the surface phosphonic acid groups, resulting in weaker attraction with the iodide anion than is observed with Zr-**RuP^6**@Pt/$K_xH_{4-x}Nb_6O_{17}$. Although **RuCP^2**-Zr-**RuP^6**@Pt/$K_xH_{4-x}Nb_6O_{17}$ showed a large negative shift following the addition of the iodide (+32 mV → ±0.0 mV), implying attraction of the iodide anions, the photocatalytic activity was the lowest among the three PS-double-layered photocatalysts. Since the surface of **RuCP^2**-Zr-**RuP^6**@Pt/$K_xH_{4-x}Nb_6O_{17}$ has no interactive functional groups for iodide anions (52,53), the electrostatic attraction between the surface-immobilized $[Ru^{2+}(bpy)_3]$-type molecules and iodide anions is less effective for electron donation from the iodide ions compared to that between the surface Zr^{4+}-phosphonates and iodides.

The amount of oxidized iodide species was determined from the UV-vis absorption spectrum of the supernatant solution after each reaction (Figure S7). All solutions showed two characteristic triiodide anion (I_3^-) absorption bands at 290 and 350 nm (52,55,56). Table S4 summarizes the amounts of I_3^- produced for each reaction. Although their precise quantitative determination was difficult, owing to light scattering by the residual particles ever after ultracentrifugation, the produced I_3^- amount approached the stoichiometric values of the evolved H_2. Thus, we concluded that the iodide acted as the electron source for proton reduction to evolve H_2, as expressed in Eq. I:

$$2H^+ + 3I^- \rightarrow H_2 + I_3^- \tag{I}$$

Notably, I_3^- production generally causes a gradual decrease in the H_2 production rate, as observed in each reaction during 6 h light irradiation (Figure 2), attributed to its light shielding effect. The absorbance values of the 20-fold diluted supernatant solutions of Zr-**RuCP^6**-Zr-**RuP^6**@Pt/$K_xH_{4-x}Nb_6O_{17}$ and **RuCP^6**-Zr-**RuP^6**@Pt/$K_xH_{4-x}Nb_6O_{17}$ at 470 nm were 0.07 and 0.06, respectively, indicating that the actual absorbance of the reaction solution is >1 (Table S4).

Apparent quantum yields for H$_2$ evolution in the KI system

The AQYs after 6 h irradiation of Zr-**RuCP^6**-Zr-**RuP^6**@Pt/$K_xH_{4-x}Nb_6O_{17}$ and **RuCP^6**-Zr-**RuP^6**@Pt/$K_xH_{4-x}Nb_6O_{17}$ were estimated to be 0.38% and 0.29%, respectively. These values are slightly smaller but comparable to the values of our previously reported Pt-TiO_2 nanoparticles with the same PS-double-layered structure (AQY = 0.54% for Zr-**RuCP^6**-Zr-**RuP^6**@1wt%Pt-TiO_2 and 0.30% for **RuCP^6**-Zr-**RuP^6**@1wt%Pt-TiO_2)(48). In contrast, the AQY of **RuCP^2**-Zr-**RuP^6**@Pt/$K_xH_{4-x}Nb_6O_{17}$ (0.054%), which does not comprise any surface phosphonate groups, was double that of the corresponding Pt-TiO_2 nanoparticle (0.028%, **RuCP^2**-Zr-**RuP^6**@1wt%Pt-TiO_2). Similarly, the PS-single-layered **RuCP^2**@Pt/$K_xH_{4-x}Nb_6O_{17}$ photocatalytically evolved H_2 (TON = 2.36, AQY= 0.020%), while the Pt-TiO_2 nanoparticle with the same **RuCP^2** dye was almost inactive (TON = 0.28, AQY = 0.0024%). These differences between Pt/$K_xH_{4-x}Nb_6O_{17}$ and Pt-TiO_2 are ascribable to the size relationship between the Pt cocatalyst and Ru(II)-dye layer. As discussed in various literature reports (41,44), the Pt cocatalysts in Pt/$K_xH_{4-x}Nb_6O_{17}$ were incorporated into the $K_xH_{4-x}Nb_6O_{17}$ interlayer and the Pt surface was barely exposed to the solid–solution interface, while the Pt cocatalyst loaded on the TiO_2 nanoparticle was directly exposed to the interface. On the other hand, the thickness of the Ru(II)-dye double layer comprising surface phosphonate or Zr^{4+}-phosphonate groups, roughly estimated at 3–4 nm based on the molecular sizes of the immobilized Ru(II) dyes, was slightly larger than the size of the Pt cocatalyst (~2.9 nm) loaded on the TiO_2 nanoparticle (48). These sizes indicate that the Pt cocatalysts loaded on TiO_2 were submerged in the Ru(II)-dye double layer and the Pt surface was barely exposed to the particle–solution interface, especially for the thickest layer Zr-**RuCP^6**-Zr-**RuP^6**@1wt%Pt-TiO_2. The photocatalytic activity is therefore comparable to that of the Pt/$K_xH_{4-x}Nb_6O_{17}$ particle with the same dye double layer structure. Thus, to suppress the back reaction on the Pt cocatalyst surface, double layering of Ru(II) dyes using Zr^{4+} cations is comparably effective to the intercalation of a Pt cocatalyst into the interlayer of a semiconductor substrate. This technique shows great potential for application to other semiconductor photocatalysts. Further, the significant enhancement of the photocatalytic activity of a Pt/$K_xH_{4-x}Nb_6O_{17}$

particle by changing the surface structure of the Ru(II)-dye double layer from simple bpy to phosphonate or Zr^{4+}-phosphonate-functionalized bpy clearly indicates the importance of surface structure for photocatalytic H_2 evolution activity.

Photocatalytic H_2 evolution reaction using $[Co(bpy)_3]SO_4$ as cationic electron donor

To further investigate the impact of the surface structure on the H_2 evolution efficiency, the reaction was next conducted with $[Co(bpy)_3]SO_4$ aqueous solution instead of KI. In this case we predicted that the cationic $[Co(bpy)_3]^{2+}$ complex acts as a cationic one-electron donor, which completely differs from the process with the iodide anion. In addition, this complex molecule is too large to approach the Pt cocatalyst immobilized in the interlayer of $K_xH_{4-x}Nb_6O_{17}$. Thus, back electron transfer to the oxidized electron donor $[Co(bpy)_3]^{3+}$ is completely suppressed. Figure 3 shows the time courses of H_2 evolution from 16.4 mM $[Co(bpy)_3]SO_4$ aqueous solution (pH = 2, acidified by adding aqueous HCl); the results are also summarized in Table 2. No hydrogen evolution was observed in the absence of Ru(II) PS, light, or $[Co(bpy)_3]^{2+}$ electron donor (Table S2).
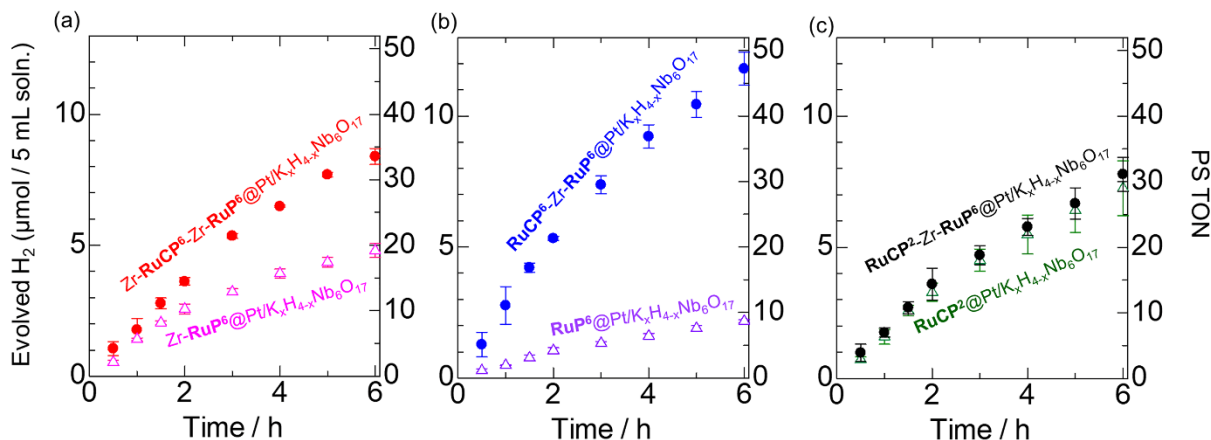

Figure 3. Photocatalytic H_2 evolution reactions driven by (a) Zr-**RuCP⁶**-Zr-**RuP⁶**@Pt/$K_xH_{4-x}Nb_6O_{17}$ (red closed circles) and Zr-**RuP⁶**@Pt/$K_xH_{4-x}Nb_6O_{17}$ (pink open triangles), (b) **RuCP⁶**-Zr-**RuP⁶**@Pt/$K_xH_{4-x}Nb_6O_{17}$ (blue closed triangles) and **RuP⁶**@Pt/$K_xH_{4-x}Nb_6O_{17}$ (purple open triangles), and (c) **RuCP²**-Zr-**RuP⁶**@Pt/$K_xH_{4-x}Nb_6O_{17}$ (black closed circles) and **RuCP²**@Pt/$K_xH_{4-x}Nb_6O_{17}$ (green open circles) in the presence of 100 µM Ru(II) dye and 16.4 mM $[Co(bpy)_3]SO_4$ as the electron donor (initial pH = 2.0, λ = 470 ± 10 nm).

Table 2. Results of photocatalytic H_2 evolution experiments in $[Co(bpy)_3]SO_4$ aqueous solution.

Photocatalyst	$[Co(bpy)_3]SO_4$ (mM)	H_2 (µmol) (0–6 h)	PS TON[a] (0–3 h)	PS TON[a] (0–6 h)	PS initial TOF[a]	AQY[a] (%) (0–6 h)	iAQY[a] (%) (0–1 h)
RuCP²@Pt/$K_xH_{4-x}Nb_6O_{17}$	16.4	7.25±1.04	18.0	29.0	6.3	0.24	0.32
RuP⁶@Pt/$K_xH_{4-x}Nb_6O_{17}$	16.4	2.17±0.06	5.29	8.68	1.9	0.07	0.10
Zr-**RuP⁶**@Pt/$K_xH_{4-x}Nb_6O_{17}$	16.4	4.80±0.26	12.9	19.2	5.6	0.16	0.28
RuCP²-Zr-**RuP⁶**@Pt/$K_xH_{4-x}Nb_6O_{17}$	16.4	7.79±0.65	18.8	31.1	7.0	0.26	0.35
RuCP⁶-Zr-**RuP⁶**@Pt/$K_xH_{4-x}Nb_6O_{17}$	16.4	11.8±0.63	29.5	47.2	11	0.40	0.56
RuCP⁶-Zr-**RuP⁶**@Pt/$K_xH_{4-x}Nb_6O_{17}$	1.64	4.15±0.01	14.8	16.6	7.9	-	0.40
RuCP⁶-Zr-**RuP⁶**@Pt/$K_xH_{4-x}Nb_6O_{17}$ -2nd	1.64	4.04±0.21	13.7	16.2	5.3	-	0.27
Zr-**RuCP⁶**-Zr-**RuP⁶**@Pt/$K_xH_{4-x}Nb_6O_{17}$	16.4	8.39±0.30	21.4	33.6	7.1	0.28	0.36

[a]Measurement conditions: [Ru-PS] = 100 µM in total, HCl aqueous solution (pH = 2), λ_{ex} = 470 ± 10 nm, 70 mW. The reaction solution was purged by Ar-bubbling for 1 h before light irradiation. The numerical values are averages of more than three experiments. Definitions: TON, turn-over number; TOF, turn-over frequency; AQY, apparent quantum yield. Average value of produced H_2 was used in these calculations.

^1H NMR spectrum after the 6 h reaction of **RuCP⁶**-Zr-**RuP⁶**@Pt/$K_xH_{4-x}Nb_6O_{17}$ clearly indicates that $[Co(bpy)_3]^{3+}$ was produced as the oxidation product coupled with the H_2 evolution reaction (Figure S8). Further, no signals assignable to the

Ru(II) dyes was observed, suggesting the superior durability of the **RuCP⁶**-Zr-**RuP⁶**@Pt/K$_x$H$_{4-x}$Nb$_6$O$_{17}$. These results indicate that the [Co(bpy)$_3$]$^{2+}$ donor was one-electron-oxidized to produce the [Co(bpy)$_3$]$^{3+}$ as the result of photocatalytic H$_2$ evolution in these systems. Although we tried to estimate the amount of [Co(bpy)$_3$]$^{3+}$ by UV-Vis absorption spectral measurement (Figure S9), it was failed because the similar spectral shapes of tris-bipyridyl Co(III) and Co(II) complexes (57). The photocatalytic activity clearly depended on the surface structure. Indeed, the activity of the PS-double-layered particles increased in the order **RuCP²**-Zr-**RuP⁶**@Pt/K$_x$H$_{4-x}$Nb$_6$O$_{17}$ < Zr-**RuCP⁶**-Zr-**RuP⁶**@Pt/K$_x$H$_{4-x}$Nb$_6$O$_{17}$ < **RuCP⁶**-Zr-**RuP⁶**@Pt/K$_x$H$_{4-x}$Nb$_6$O$_{17}$. Notably, both Zr-**RuCP⁶**-Zr-**RuP⁶**@Pt/K$_x$H$_{4-x}$Nb$_6$O$_{17}$ and **RuCP⁶**-Zr-**RuP⁶**@Pt/K$_x$H$_{4-x}$Nb$_6$O$_{17}$ evolved an amount of H$_2$ comparable to that evolved from the KI system, even though the donor concentration (16.4 mM [Co(bpy)$_3$]SO$_4$) was approximately 30-fold lower than that of the iodide (0.5 M). This is probably because the redox reaction of [Co(bpy)$_3$]$^{3+/2+}$ does not accompany any interatomic bond formation reactions, as is the case with I$_3^-$/ I$^-$.

Interestingly, the TON for **RuCP⁶**-Zr-**RuP⁶**@Pt/K$_x$H$_{4-x}$Nb$_6$O$_{17}$ was 1.4 times higher than that for Zr-**RuCP⁶**-Zr-**RuP⁶**@Pt/K$_x$H$_{4-x}$Nb$_6$O$_{17}$, in contrast to the KI system (see Figure 2). The zeta potential at pH 2 for **RuCP⁶**-Zr-**RuP⁶**@Pt/K$_x$H$_{4-x}$Nb$_6$O$_{17}$ was confirmed to be near-neutral both in the sulfuric acid (−0.83 mV) and aqueous HCl (+1.0 mV, Table S3) solutions. However, the potential positively shifted by up to +6.7 mV following the addition of [Co(bpy)$_3$]$^{2+}$, suggesting that cationic [Co(bpy)$_3$]$^{2+}$ molecules were attracted near the particle surface, probably through electrostatic attraction of the partially H$^+$-released surface phosphonates of **RuCP⁶**. In contrast, the zeta potential (+2.1 mV) of Zr-**RuCP⁶**-Zr-**RuP⁶**@Pt/K$_x$H$_{4-x}$Nb$_6$O$_{17}$ in the sulfuric acid solution shifted slightly to +5.6 mV. Considering that the potential of Zr-**RuCP⁶**-Zr-**RuP⁶**@Pt/K$_x$H$_{4-x}$Nb$_6$O$_{17}$ in aqueous HCl was highly positive (+31 mV), the Zr^{4+} cations bound by the surface phosphonate of **RuCP⁶** may be surrounded by sulfate anions in aqueous H$_2$SO$_4$, providing a near-neutral zeta potential. In this case, the electron donating [Co(bpy)$_3$]$^{2+}$ cations are indirectly attracted by the sulfate anions surrounding the surface Zr^{4+} cations. The electron transfer kinetics is inversely proportional to the square of the distance between the electron donor and accepter. Thus, the plausible origin of the higher H$_2$ evolution activity in the [Co(bpy)$_3$]$^{2+}$ solution of **RuCP⁶**-Zr-**RuP⁶**@Pt/K$_x$H$_{4-x}$Nb$_6$O$_{17}$ over that in Zr-**RuCP⁶**-Zr-**RuP⁶**@Pt/K$_x$H$_{4-x}$Nb$_6$O$_{17}$ is due to the closer distance between the cationic [Co(bpy)$_3$]$^{2+}$ donor and **RuCP⁶** on the particle surface with direct electrostatic interaction with the anionic phosphonates. On the other hand, **RuCP²**-Zr-**RuP⁶**@Pt/K$_x$H$_{4-x}$Nb$_6$O$_{17}$, which exhibited the lowest H$_2$ evolution activity among the three PS-double-layered particles in aqueous KI, showed almost the same activity as Zr-**RuCP⁶**-Zr-**RuP⁶**@Pt/K$_x$H$_{4-x}$Nb$_6$O$_{17}$ when [Co(bpy)$_3$]$^{2+}$ was used instead. This possibly originates from the difference in the electron donating process: [Co(bpy)$_3$]$^{2+}$ donates one electron to form the stable Co(III) species, whereas electron donation from the iodide anion is accompanied by two I–I bond formations to form the stable I$_3^-$ anion. Thus, a high donor concentration is not required for [Co(bpy)$_3$]$^{2+}$ to donate one electron to the surface Ru(II)-PS, as mentioned above. The change in the zeta potential shift of **RuCP²**-Zr-**RuP⁶**@Pt/K$_x$H$_{4-x}$Nb$_6$O$_{17}$, following the addition of [Co(bpy)$_3$]$^{2+}$ (+11 mV → +17 mV) was similar to that of Zr-**RuCP⁶**-Zr-**RuP⁶**@Pt/K$_x$H$_{4-x}$Nb$_6$O$_{17}$, and is consistent with their comparable photocatalytic activities in the [Co(bpy)$_3$]$^{2+}$ donor solution. These results suggest that the appropriate surface modification of a photocatalyst particle to induce the desirable electrostatic attraction with redox mediators shows great potential as an effective strategy for boosting the electron donation from the mediators to the PS molecules. Although the dominant reason for the similar activity between the PS-single-layered **RuCP²**@Pt/K$_x$H$_{4-x}$Nb$_6$O$_{17}$ and PS-double-layered **RuCP²**-Zr-**RuP⁶**@Pt/K$_x$H$_{4-x}$Nb$_6$O$_{17}$ is unclear at present, it might be due to the difference in the amount of Ru(II) dyes immobilized directly on the surface of K$_x$H$_{4-x}$Nb$_6$O$_{17}$.

Complete consumption of [Co(bpy)₃]²⁺ donor

We also performed the photocatalytic hydrogen evolution reaction using **RuCP⁶**-Zr-**RuP⁶**@Pt/K$_x$H$_{4-x}$Nb$_6$O$_{17}$ in a 10-fold lower concentration of [Co(bpy)$_3$]SO$_4$ (1.64 mM) solution to avoid light absorption by the [Co(bpy)$_3$]$^{3+/2+}$ mediators, which interferes with the light absorption of Ru(II) PSs (Figure 4).
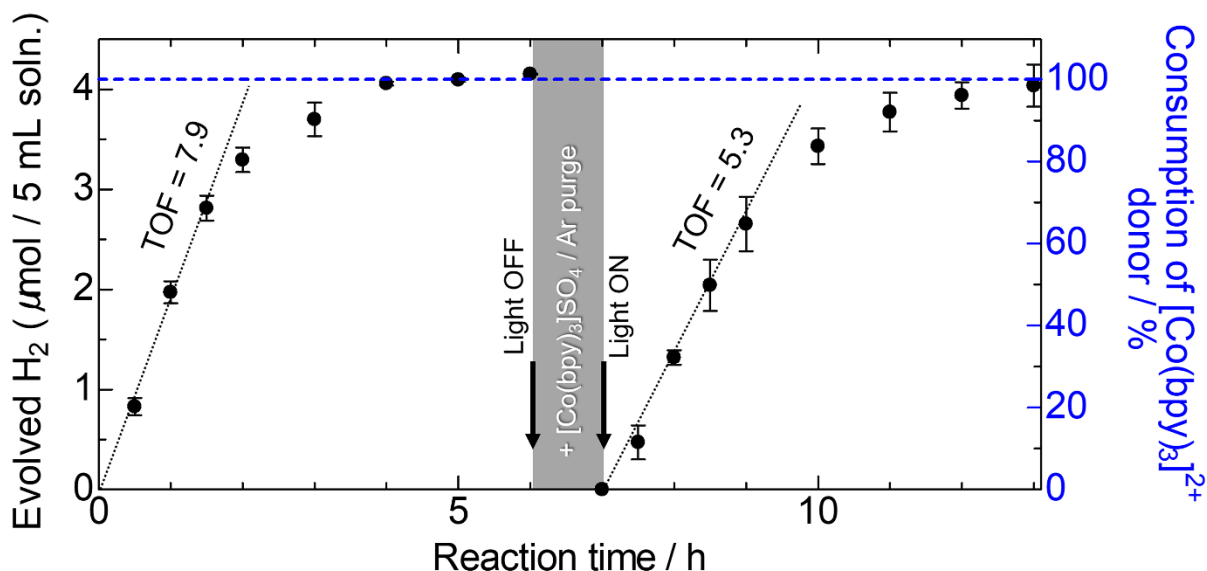
Figure 4. Two-cycle photocatalytic hydrogen production reactions using **RuCP^6**-Zr-**RuP^6**@Pt/$K_xH_{4-x}Nb_6O_{17}$ in the presence of 100 μM Ru(II) dye and 1.64 mM [Co(bpy)$_3$]SO$_4$ as the electron donor (initial pH = 2.0, λ = 470 ± 10 nm).

Even at this low donor concentration, the initial 1 h TOF approximated 70% in 16.4 mM donor solution, indicating the superior performance of this PS-double-layered photocatalyst. Notably, the evolved amount of H$_2$ after 4 h light irradiation reached approximately 4.1 μmol, which is nearly equal to the upper limit of evolved hydrogen from the total 8.2 μmol of the one-electron [Co(bpy)$_3$]$^{2+}$ donor. This finding strongly suggests that **RuCP^6**-Zr-**RuP^6**@Pt/$K_xH_{4-x}Nb_6O_{17}$ can drive the photocatalytic H$_2$ evolution reaction until all the [Co(bpy)$_3$]$^{2+}$ donors are oxidized to [Co(bpy)$_3$]$^{3+}$. ^{1}H NMR spectrum of the supernatant solution in the presence of three internal standards (Acetone, MeCN, and 1,4-dioxane) suggests that about 2 mM [Co(bpy)$_3$]$^{3+}$ was produced after 6 h irradiation (Figure S10 and Table S5). This spectrum with sharp signals is strong evidence showing that all paramagnetic [Co(bpy)$_3$]$^{2+}$ electron donors (1.64 mM) were completely oxidized during the photochemical H$_2$ evolution reaction. The photocatalytic reaction was next conducted by adding another 8.2 μmol [Co(bpy)$_3$]SO$_4$ followed by Ar-purging. Although the initial TOF in the second cycle was slightly lowered to ~70%, the amount of evolved H$_2$ still reached ~4 μmol, indicating the complete consumption of the [Co(bpy)$_3$]$^{2+}$ donor, even in the presence of 8.2 μmol of the one-electron oxidized [Co(bpy)$_3$]$^{3+}$ in the initial period. The lower activity in the second cycle compared to that in the first cycle was attributed to back electron transfer to the oxidized donor [Co(bpy)$_3$]$^{3+}$. Compared to the divalent species, the trivalent species is more effectively attracted near the particle surface by electrostatic interaction and thus, backward electron transfer occurs to some extent. Nevertheless, the H$_2$ evolution continued until another portion of [Co(bpy)$_3$]$^{2+}$ was completely oxidized. Therefore, the charge separation process triggered by the energy transfer process from the outer excited **RuCP^{6*}** to inner **RuP^6** followed by the electron injection process from the inner excited **RuP^{6*}** to Pt/$K_xH_{4-x}Nb_6O_{17}$ is relatively faster than the back electron transfer from the outer excited **RuCP^{6*}** to the oxidized [Co(bpy)$_3$]$^{3+}$, resulting in the complete consumption of the secondary added [Co(bpy)$_3$]$^{2+}$ donors.

CONCLUSION

In this work, to suppress the back electron transfer processes that occur from a H$_2$ evolving photocatalyst to an oxidized redox mediator, we synthesized new hybrid photocatalysts composed of the internally platinated layered niobate Pt/$K_xH_{4-x}Nb_6O_{17}$ and surface-immobilized double-layered Ru(II) photosensitizers with phosphonates coordinated to Zr^{4+} cations. As expected from the pioneering works on layered niobates (41,43,44), the photocatalytic H$_2$ evolution activity (e.g., AQY) of the single-PS-layered photocatalyst **RuCP^2**@Pt/$K_xH_{4-x}Nb_6O_{17}$ in the presence of the KI redox-reversible electron do-

nor was approximately 10 times higher than that of its TiO$_2$ analogue (**RuCP^2**@Pt/TiO$_2$) (48). This occurred because intercalation of the Pt-cocatalyst effectively suppressed back reaction with the oxidized mediators on the Pt cocatalyst surface. The double-layering of Ru(II) PS on the Pt/$K_xH_{4-x}Nb_6O_{17}$ surface significantly improved the photocatalytic H$_2$ evolution activity probably by enhancing the charge separation efficiency between the electron-injected semiconductor and photo-oxidized PS, as is the case with Pt-TiO$_2$ nanoparticles. The photocatalytic activity of the PS-double-layered Pt/$K_xH_{4-x}Nb_6O_{17}$ system strongly depended on the surface structure. Thus, Zr-**RuCP^6**-Zr-**RuP^6**@Pt/$K_xH_{4-x}Nb_6O_{17}$, with Zr^{4+} cations on its surface, showed the highest AQY (0.38%) in the KI aqueous solution, while **RuCP^6**-Zr-**RuP^6**@Pt/$K_xH_{4-x}Nb_6O_{17}$, having phosphonate anions on its surface, exhibited the highest AQY (0.40%) in the [Co(bpy)$_3$]SO$_4$ aqueous solution. These results suggest that surface modification of dye-sensitized photocatalysts to modify the electrostatic interaction between the photocatalyst surface and redox mediator is a promising approach not only to enhance electron donation but also to suppress back electron transfer to the redox mediator. In fact, **RuCP^6**-Zr-**RuP^6**@Pt/$K_xH_{4-x}Nb_6O_{17}$ was photocatalytically active even in a 10-fold lower [Co(bpy)$_3$]SO$_4$ solution concentration, and almost all the [Co(bpy)$_3$]$^{2+}$ donors were consumed as an electron source for H$_2$ evolution. These results are important for the fabrication of Z-scheme water splitting photocatalysts, because back electron transfer to the oxidized redox mediator on a H$_2$ evolution photocatalyst is a bottleneck issue. In conclusion, the combination of two nano-architectures, the intercalation of a Pt cocatalyst and PS double layering, can suppress back electron transfer to the oxidized redox mediator and shows potential as an effective approach for the preparation of highly active Z-scheme water splitting photocatalysts. Further study to design a water-splitting Z-scheme photocatalyst based on a PS-multilayered H$_2$ evolution photocatalyst is in progress.

EXPERIMENTAL SECTION

Materials and Syntheses

Caution! Although we did not come across any difficulties, most of the chemicals used in this study are potentially harmful and should be used in small quantities and handled with care in a fumehood. All commercially available starting materials were used as received without further purification. The internally platinated layered niobate Pt/$K_xH_{4-x}Nb_6O_{17}$ was synthesized according to a previously reported method (41) with some modifications. The Ru(II) molecular photosensitizers (**RuCP^2**, **RuCP^6**, and **RuP^6**) (49, 58) were also synthesized using previously reported methods.

Preparation of the Ru(II)-dye-immobilized Pt/K$_x$H$_{4-x}$Nb$_6$O$_{17}$

Six types of Ru(II)-dye-immobilized Pt/K$_x$H$_{4-x}$Nb$_6$O$_{17}$ nanoparticles (**RuCP^2**@Pt/K$_x$H$_{4-x}$Nb$_6$O$_{17}$, **RuP^6**@Pt/K$_x$H$_{4-x}$Nb$_6$O$_{17}$, Zr-**RuP^6**@Pt/K$_x$H$_{4-x}$Nb$_6$O$_{17}$, **RuCP^2**-Zr-**RuP^6**@Pt/K$_x$H$_{4-x}$Nb$_6$O$_{17}$, **RuCP^6**-Zr-**RuP^6**@Pt/K$_x$H$_{4-x}$Nb$_6$O$_{17}$, and Zr-**RuCP^6**-Zr-**RuP^6**@Pt/K$_x$H$_{4-x}$Nb$_6$O$_{17}$) were synthesized according to our previously reported procedure (48) for Ru(II)-dye-immobilized Pt-TiO$_2$ nanoparticles with several modifications as follows:

I. Immobilization of the first Ru(II)-dye layer. Exactly, 30 mg of Pt/K$_x$H$_{4-x}$Nb$_6$O$_{17}$ was dispersed in 2.5 mM Ru(II)-dye solution (**RuCP^2** or **RuP^6**, 6 mL). Next, 50 µL of 34% aqueous HCl solution was added to acidify the dispersion solution and stirred overnight at 293 K in the dark. The resultant Ru(II)-dye-immobilized Pt/K$_x$H$_{4-x}$Nb$_6$O$_{17}$ was isolated by ultracentrifugation (50,000 rpm, 15 min) and then washed twice with 0.4% aqueous HCl. The Ru(II)-dye-single-layered Pt/K$_x$H$_{4-x}$Nb$_6$O$_{17}$ (**RuCP^2**@Pt/K$_x$H$_{4-x}$Nb$_6$O$_{17}$ or **RuP^6**@Pt/K$_x$H$_{4-x}$Nb$_6$O$_{17}$) was finally obtained by drying under air at 293 K.

II. Immobilization of Zr^{4+} cations on the phosphonates of the Ru(II) dyes. The well-dried **RuP^6**@Pt/K$_x$H$_{4-x}$Nb$_6$O$_{17}$ was dispersed in 6 mL of an MeOH solution of 50 mM ZrCl$_2$O·8H$_2$O and stirred overnight at 293 K in the dark. The dispersed particles were collected by ultracentrifugation (50,000 rpm, 15 min), washed twice with MeOH, and then dried under air for several days to afford the orange Zr-**RuP^6**@Pt/K$_x$H$_{4-x}$Nb$_6$O$_{17}$.

III. Immobilization of the second Ru(II)-dye layer. The second immobilization of the Ru(II) dye was conducted using an almost identical procedure to that used for the first dye layer immobilization, but using Zr-**RuP^6**@Pt/K$_x$H$_{4-x}$Nb$_6$O$_{17}$ instead of Pt/K$_x$H$_{4-x}$Nb$_6$O$_{17}$. Briefly, Zr-**RuP^6**@Pt/K$_x$H$_{4-x}$Nb$_6$O$_{17}$ was dispersed in 2.5 mM Ru(II)-dye solution (**RuCP^2** or **RuCP^6**, 6 mL) and then acidified with 50 µL of 34% aqueous HCl solution. After stirring overnight at 293 K in the dark, the dispersed particles were isolated by ultracentrifugation (50,000 rpm, 15 min) and then washed twice with 0.4% aqueous HCl. The Ru(II)-dye double-layered particles (**RuCP^2**-Zr-**RuP^6**@Pt/K$_x$H$_{4-x}$Nb$_6$O$_{17}$ or **RuCP^6**-Zr-**RuP^6**@Pt/K$_x$H$_{4-x}$Nb$_6$O$_{17}$) were obtained by drying under air for several days at 293 K. Subsequently, **RuCP^6**-Zr-**RuP^6**@Pt/K$_x$H$_{4-x}$Nb$_6$O$_{17}$ was treated with ZrCl$_2$O·8H$_2$O MeOH solution (method II above) to form the Zr^{4+}-cation-modified Ru(II)-dye double-layered Zr-**RuCP^6**-Zr-**RuP^6**@Pt/K$_x$H$_{4-x}$Nb$_6$O$_{17}$ particles.

The immobilized amounts of Ru(II) dyes were estimated from the UV-vis absorption spectrum of each supernatant solution, isolated by ultracentrifugation of the Ru(II)-dye immobilization reaction (see the ESI for details).

Measurements

^{1}H-NMR spectra were recorded at 293 K on an JEOL ECZ-400S NMR spectrometer, while UV−vis absorption spectra were recorded on a Shimadzu UV-2400PC spectrophotometer. Luminescence spectra were recorded on a JASCO FP-6600 or FP-8600 spectrofluorometer at 298 K. Each sample solution was deoxygenated by N$_2$ bubbling for 30 min at 298 K. Emission lifetime measurements were conducted using a Quantaurus-Tau C11367 fluorescence lifetime spectrometer (Hamamatsu Photonics KK) excited by a UV light-emitting diode (LED) light source (λ_{ex} = 280 nm). Energy-dispersive XRF spectra were recorded using a Bruker S2 PUMA analyzer. Powder X-

ray diffraction studies were conducted using a Rigaku SPD diffractometer at beamline BL-8B of the Photon Factory, KEK, Japan. The wavelength of the synchrotron X-ray was 1.5372(1) Å. TEM was performed using a JEOL JEM-2010x electron microscope (200 kV).

Photocatalytic water reduction reaction

This reaction was conducted in the dark. A KI (0.5 M, pH = 2 adjusted by adding aqueous HCl) or [Co(bpy)$_3$]SO$_4$ (16.4 mM or 1.64 mM, pH = 2 adjusted by adding aqueous HCl) solution containing Ru(II)-dye-immobilized particles (100 µM) was placed into an in-house Schlenk flask-equipped quartz cell (volume: 265 mL) with a small magnetic stirring bar. Each sample flask was doubly sealed with rubber septa, and the mixed solution was deoxygenated by Ar-bubbling for 1 h. The flask was then irradiated from the bottom with a blue LED lamp (λ = 470 ± 10 nm; 70 mW; Opto Device Lab. Ltd., OP6-4710HP2). The temperature was controlled at 293 K using an in-house aluminum water-cooling jacket with a water-circulating temperature controller (EYELA CCA-1111). The gas samples (0.6 mL) for each analysis were then collected from the headspace using a gas-tight syringe (Valco Instruments Co. Inc.), and the amount of evolved H$_2$ was determined using a gas chromatograph (Agilent 490 Micro Gas). The turn-over numbers (TONs) and turn-over frequencies (TOFs) were estimated from the amount of evolved H$_2$, which required two photoredox cycles of the Ru(II) photosensitizer to reduce one water molecule. Each photocatalytic H$_2$ evolution reaction was conducted threefold under the same conditions, and the average value with standard deviation was recorded. The detection limit of the H$_2$ gas chromatography analysis was 0.005 µmol. The AQY was calculated using the equation:

$$\text{AQY} = N_e/N_p = 2N_{H2}/N_p$$

where N_e represents the number of reacted electrons, N_{H2} is the number of evolved H$_2$ molecules, and N_p is the number of incident photons.

ASSOCIATED CONTENT

Supporting Information. Experimental details of the Ru(II) dye immobilized on the Pt/K$_x$H$_{4-x}$Nb$_6$O$_{17}$ surface; UV-vis absorption spectra of all supernatant solutions obtained from the syntheses of Ru(II)-dye-immobilized Pt/K$_x$H$_{4-x}$Nb$_6$O$_{17}$ particles; XRF spectra, PXRD patterns, and TEM images of Pt/K$_x$H$_{4-x}$Nb$_6$O$_{17}$ particles; ^{1}H NMR and emission spectra of the supernatant solution obtained from the preparation of **RuCP^6**-Zr-**RuP^6**@Pt/K$_x$H$_{4-x}$Nb$_6$O$_{17}$; control experiments of photocatalytic H$_2$ evolution reaction; zeta potentials of Ru(II)-dye-immobilized Pt/K$_x$H$_{4-x}$Nb$_6$O$_{17}$ particles; estimated absorbance for I$_3^-$ and Ru(II) dyes in the reaction solutions; ^{1}H NMR spectrum of the reaction solution of **RuCP^6**-Zr-**RuP^6**@Pt/K$_x$H$_{4-x}$Nb$_6$O$_{17}$ in the [Co(bpy)$_3$]$^{2+}$ aqueous solution. This material is available free of charge via the Internet at http://pubs.acs.org.

AUTHOR INFORMATION

Corresponding Authors

*E-mail: akoba@sci.hokudai.ac.jp (A.K.).

Present Addresses

†Department of Applied Chemistry for Environment, School of Biological and Environmental Sciences, Kwansei Gakuin University, 2-1 Gakuen, Sanda, Hyogo 669-1337, Japan.

Author Contributions

The manuscript was written through contributions of all authors. All authors have given approval to the final version of the manuscript.

Funding Sources

ACKNOWLEDGMENT

REFERENCES

1.   Acharya, S.; Padhi, D. K.; Parida, K. M. Visible Light Driven LaFeO₃ Nano Sphere/RGO Composite Photocatalysts for Efficient Water Decomposition Reaction. *Catal. Today* **2020**, *353*, 220–231.

2.   Graetzel, M. Artificial Photosynthesis: Water Cleavage into Hydrogen and Oxygen by Visible Light. *Acc. Chem. Res.* **1981**, *14*, 376–384.

3.   Ma, Y.; Wang, X.; Jia, Y.; Chen, X.; Han, H.; Li, C. Titanium Dioxide-Based Nanomaterials for Photocatalytic Fuel Generations. *Chem. Rev.* **2014**, *114*, 9987–10043.

4.   Kudo, A.; Miseki, Y. Heterogeneous Photocatalyst Materials for Water Splitting. *Chem. Soc. Rev.* **2009**, *38*, 253–278.

5.   Fang, X.; Kalathil, S.; Reisner, E. Semi-Biological Approaches to Solar-to-Chemical Conversion. *Chem. Soc. Rev.* **2020**, *49* (14), 4926–4952.

6.   Fujishima, A.; Honda, K. Electrochemical Photolysis of Water at a Semiconductor Electrode. *Nature* **1972**, *238*, 37–38.

7.   Huang, H.; Pradhan, B.; Hofkens, J.; Roeffaers, M. B. J.; Steele, J. A. Solar-Driven Metal Halide Perovskite Photocatalysis: Design, Stability, and Performance. *A.C.S. Energy Lett.* **2020**, *5*, 1107–1123.

8.   Niu, F.; Wang, D.; Li, F.; Liu, Y.; Shen, S.; Meyer, T. J. Hybrid Photoelectrochemical Water Splitting Systems: From Interface Design to System Assembly. *Adv. Energy Mater.* **2020**, *10*, 1900399.

9.   Ju, L.; Shang, J.; Tang, X.; Kou, L. Tunable Photocatalytic Water Splitting by the Ferroelectric Switch in a 2D AgBiP₂Se₆ Monolayer. *J. Am. Chem. Soc.* **2020**, *142*, 1492–1500.

10.   Yu, H.; Jiang, L.; Wang, H.; Huang, B.; Yuan, X.; Huang, J.; Zhang, J.; Zeng, G. Modulation of Bi₂MoO₆-Based Materials for Photocatalytic Water Splitting and Environmental Application: A Critical Review. *Small* **2019**, *15*, 1901008.

11.   Wang, Q.; Nakabayashi, M.; Hisatomi, T.; Sun, S.; Akiyama, S.; Wang, Z.; Pan, Z.; Xiao, X.; Watanabe, T.; Yamada, T.; Shibata, N.; Takata, T.; Domen, K. Oxysulfide Photocatalyst for Visible-Light-Driven Overall Water Splitting. *Nat. Mater.* **2019**, *18*, 827–832.

12.   Xu, C. P.; Ravi Anusuyadevi, P. R.; Aymonier, C.; Luque, R.; Marre, S. Nanostructured Materials for Photocatalysis. *Chem. Soc. Rev.* **2019**, *48*, 3868–3902.

13.   Hisatomi, T.; Domen, K. Reaction Systems for Solar Hydrogen Production via Water Splitting with Particulate Semiconductor Photocatalysts. *Nat. Catal.* **2019**, *2*, 387–399.

14.   Iwashina, K.; Kudo, A. Rh-Doped SrTiO₃ Photocatalyst Electrode Showing Cathodic Photocurrent for Water Splitting under Visible-Light Irradiation. *J. Am. Chem. Soc.* **2011**, *133*, 13272–13275.

15.   Wang, Q.; Hisatomi, T.; Jia, Q. X.; Tokudome, H.; Zhong, M.; Wang, C. Z.; Pan, Z. H.; Takata, T.; Nakabayashi, M.; Shibata, N.; Li, Y. B.; Sharp, I. D.; Kudo, A.; Yamada, T.; Domen, K. Scalable Water Splitting on Particulate Photocatalyst Sheets with a Solar-to-Hydrogen Energy Conversion Efficiency Exceeding 1%. *Nat. Mater.* **2016**, *15*, 611–615.

16.   Takata, T.; Jiang, J. Z.; Sakata, Y.; Nakabayashi, M.; Shibata, N.; Nandal, V.; Seki, K.; Hisatomi, T.; Domen, K. Photocatalytic Water Splitting with a Quantum Efficiency of Almost Unity. *Nature* **2020**, *581*, 411–414.

17.   Mu, L.; Zhao, Y.; Li, A.; Wang, S.; Wang, Z.; Yang, J.; Wang, Y.; Liu, T.; Chen, R.; Zhu, J.; Fan, F.; Li, R.; Li, C. Enhancing Charge Separation on High Symmetry SrTiO₃ Exposed with Anisotropic Facets for Photocatalytic Water Splitting. *Energy Environ.* **2016**, *9* (7), 2463–2469.

18.   Li, R.; Han, H.; Zhang, F.; Wang, D.; Li, C. Highly Efficient Photocatalysts Constructed by Rational Assembly of Dual-Cocatalysts Separately on Different Facets of BiVO₄. *Energy Environ.* **2014**, *7*, 1369–1376.

19.   Ma, G.; Chen, S.; Kuang, Y.; Akiyama, S.; Hisatomi, T.; Nakabayashi, M.; Shibata, N.; Katayama, M.; Minegishi, T.; Domen, K. Visible Light-Driven Z-Scheme Water Splitting Using Oxysulfide H₂ Evolution Photocatalysts. *J. Phys. Chem. Lett.* **2016**, *7*, 3892–3896.

20.   Nakada, A.; Nishioka, S.; Vequizo, J. J. M.; Muraoka, K.; Kanazawa, T.; Yamakata, A.; Nozawa, S.; Kumagai, H.; Adachi, S.; Ishitani, O.; Maeda, K. Solar-Driven Z-Scheme Water Splitting Using Tantalum/Nitrogen Co-Doped Rutile titania Nanorod as an Oxygen Evolution Photocatalyst. *J. Mater. Chem. A* **2017**, *5*, 11710–11719.

21.   Fang, M. J.; Tsao, C. W.; Hsu, Y. J. Semiconductor Nano-heterostructures for Photoconversion Applications. *J. Phys. D: Appl. Phys.* **2020**, *53*, 143001-1430033.

22.   Kumagai, H.; Aoyagi, R.; Kato, K.; Yamakata, A.; Kakihata, M.; Kato, H. Utilization of Perovskite-Type Oxynitride La₀.₅Sr₀.₅Ta₀.₅Ti₀.₅O₂N as an O₂-Evolving Photocatalyst in Z-Scheme Water Splitting. *ACS Appl. Energy Mater.* **2021**, 2056–2060.

23.   Wang, Y.; Suzuki, H.; Xie, J.; Tomita, O.; Martin, D. J.; Higashi, M.; Kong, D.; Abe, R.; Tang, J. Mimicking Natural Photosynthesis: Solar to Renewable H₂ Fuel Synthesis by Z-Scheme Water Splitting Systems. *Chem. Rev.* **2018**, *118*, 5201–5241.

24.   Wang, Q.; Domen, K. Particulate Photocatalysts for Light-Driven Water Splitting: Mechanisms, Challenges, and Design Strategies. *Chem. Rev.* **2020**, *120*, 919–985.

25.   Ng, B. J.; Putri, L. K.; Kong, X. Y.; Teh, Y. W.; Pasbakhsh, P.; Chai, S. P. Z-Scheme Photocatalytic Systems for Solar Water Splitting. *Adv. Sci. (Weinh)* **2020**, *7*, 1903171.

26.   Nakada, A.; Uchiyama, T.; Kawakami, N.; Sahara, G.; Nishioka, S.; Kamata, R.; Kumagai, H.; Ishitani, O.; Uchimoto, Y.; Maeda, K. Solar Water Oxidation by Visible-Light-Responsive Tantalum/Nitrogen-Codoped Rutile TiO₂ Anode for Photoelectrochemical Overall Water Splitting and CO₂ Fixation. *ChemPhotoChem* **2019**, *3*, 37–45.

27.   Sheridan, M. V.; Wang, Y.; Wang, D.; Troian-Gautier, L. T.; Dares, C. J.; Sherman, B. D.; Meyer, T. J. Light-Driven Water Splitting Mediated by Photogenerated Bromine. *Angew. Chem. Int. Ed. Engl.* **2018**, *57*, 3449–3453.

28.   Warnan, J.; Willkomm, J.; Ng, J. N.; Godin, R.; Prantl, S.; Durrant, J. R.; Reisner, E. Solar H₂ Evolution in Water with Modified Diketopyrrolopyrrole Dyes Immobilised on Molecular Co and Ni Catalyst–TiO₂ Hybrids. *Chem. Sci.* **2017**, *8*, 3070–3079.

29.   Wang, X.; Chen, L.; Chong, S. Y.; Little, M. A.; Wu, Y.; Zhu, W. H.; Clowes, R.; Yan, Y.; Zwijnenburg, M. A.; Sprick, R. S.; Cooper, A. I. Sulfone-Containing Covalent Organic Frameworks for Photocatalytic Hydrogen Evolution from Water. *Nat. Chem.* **2018**, *10*, 1180–1189.

30.   Gueret, R.; Poulard, L.; Oshinowo, M.; Chauvin, J.; Dahmane, M.; Dupeyre, G.; Lainé, P. P.; Fortage, J.; Collomb, M. Challenging the [Ru(bpy)₃]²⁺ Photosensitizer with a Triazatriangulenium Robust Organic Dye for Visible-Light-Driven Hydrogen Production in Water. *ACS Catal.* **2018**, *8*, 3792–3802.

31.   Guo, S.; Chen, K.; Dong, R.; Zhang, Z.; Zhao, J.; Lu, T. Robust and Long-Lived Excited State Ru(II) Polyimine Photosensitizers Boost Hydrogen Production. *ACS Catal.* **2018**, *8*, 8659–8670.

32.   Da Silva, E. S. D.; Moura, N. M. M.; Neves, M. G. P. M. S.; Coutinho, A.; Prieto, M.; Silva, C. G.; Faria, J. L. Novel Hybrids of Graphitic Carbon Nitride Sensitized with Free-Base meso-tetrakis(carboxyphenyl) Porphyrins for Efficient Visible Light Photocatalytic Hydrogen Production. *Appl. Catal. B* **2018**, *221*, 56–69.

33.   Tsukamoto, T.; Takada, K.; Sakamoto, R.; Matsuoka, R.; Toyoda, R.; Maeda, H.; Yagi, T.; Nishikawa, M.; Shinjo, N.; Amano, S.; Iokawa, T.; Ishibashi, N.; Oi, T.; Kanayama, K.; Kinugawa, R.; Koda, Y.; Komura, T.; Nakajima, S.; Fukuyama, R.; Fuse, N.; Mizui, M.; Miyasaki, M.; Yamashita, Y.; Yamada, K.; Zhang, W.; Han, R.; Liu, W.; Tsubomura, T.; Nishihara, H. Coordination Nanosheets Based on Terpyridine-Zinc(II) Complexes: As Photoactive Host Materials. *J. Am. Chem. Soc.* **2017**, *139*, 5359–5366.

34.   Lee, J. S.; Won, D. I.; Jung, W. J.; Son, H. J.; Pac, C.; Kang, S. O. Widely Controllable Syngas Production by a Dye-Sensitized TiO₂ Hybrid System with Re^I and Co^{III} Catalysts under Visible-LightIrradiation. *Angew. Chem. Int. Ed. Engl.* **2017**, *56*, 976–980.

35.   Aslan, E.; Gonce, M. K.; Yigit, M. Z.; Sarilmaz, A.; Stathatos, E.; Ozel, F.; Can, M.; Patir, I. H. Photocatalytic H₂ Evolution with a Cu₂WS₄ Catalyst on a Metal freeD-π-A Organic Dye-Sensitized TiO₂. *Appl. Catal. B* **2017**, *220*, 320–327.

36.   Tiwari, A.; Krishna, N. V.; Giribabu, L.; Pal, U. Hierarchical Porous TiO₂ Embedded Unsymmetrical Zinc–Phthalocyanine Sensitizer for Visible-Light-Induced Photocatalytic H₂ Production. *J. Phys. Chem. C* **2018**, *122*, 495–502.

37.   Yu, F.; Cui, S.; Li, X.; Peng, Y.; Yu, Y.; Yun, K.; Zhang, S.; Li, J.; Liu, J.; Hua, J. Effect of Anchoring Groups on N-Annulated Perylene-Based Sensitizersfor Dye-Sensitized Solar Cells and Photocatalytic H₂ Evolution. *Dyes Pigm.* **2017**, *139*, 7–18.

38.   Sun, Y.; Sun, Y.; Dall'Agnese, C.; Wang, X.; Chen, G.; Kitao, O.; Tamiaki, H.; Sakai, K.; Ikeuchi, T.; Sasaki, S. Dyad Sensitizer of Chlorophyll with Indoline Dye for Panchromatic Photocatalytic Hydrogen Evolution. *ACS Appl. Energy Mater.* **2018**, *1*, 2813–2820.

39.   Jung, Y. H.; Shim, H. K.; Kim, H. W.; Kim, Y. L. Photochemical Hydrogen Evolution in K₄Nb₆O₁₇ Semiconductor Particles. Sensitized by Phosphonated Trisbipyridine Ruthenium Complexes. *Bull. Korean Chem. Soc.* **2007**, *28*, 921–928.

40.   Abe, R.; Sayama, K.; Arakawa, H. Dye-Sensitized Photocatalysts for Efficient Hydrogen Production from Aqueous I- Solution under Visible Light Irradiation. *J. Photochem. Photobiol. A* **2004**, *166*, 115–122.

41.   Abe, R.; Shinmei, K.; Koumura, N.; Hara, K.; Ohtani, B. Visible-Light-Induced Water Splitting Based on Two-Step Photoexcitation between Dye-Sensitized Layered Niobate and Tungsten Oxide Photocatalysts in the Presence of a Triiodide/Iodide Shuttle Redox Mediator. *J. Am. Chem. Soc.* **2013**, *135*, 16872–16884.

42.   Kim, Y. I.; Salim, S.; Huq, M. J.; Mallouk, T. E. Visible-Light Photolysis of Hydrogen Iodide Using Sensitized Layered Semiconductor Particles. *J. Am. Chem. Soc.* **1991**, *113*, 9561–9563.

43.   Kim, Y. I.; Atherton, S. J.; Brigham, E. S.; Mallouk, T. E. Sensitized Layered Metal Oxide Semiconductor Particles for Photochemical Hydrogen Evolution from Nonsacrificial Electron Donors. *J. Phys. Chem.* **1993**, *97*, 11802–11810.

44.   Abe, R.; Shinmei, K.; Hara, K.; Ohtani, B. Robust Dye-Sensitized Overall Water Splitting System with Two-Step Photoexcitation of Coumarin Dyes and Metal Oxide Semiconductors. *Chem. Commun. (Camb)* **2009**, (24), 3577–3579.

45.   Oshima, T.; Nishioka, S.; Kikuchi, Y.; Hirai, S.; Yanagisawa, K. I.; Eguchi, M.; Miseki, Y.; Yokoi, T.; Yui, T.; Kimoto, K.; Sayama, K.; Ishitani, O.; Mallouk, T. E.; Maeda, K. An Artificial Z-Scheme Constructed from Dye-Sensitized Metal Oxide Nanosheets for Visible Light-Driven Overall Water Splitting. *J. Am. Chem. Soc.* **2020**, *142*, 8412–8420.

46.   Yoshimura, N.; Kobayashi, A.; Yoshida, M.; Kato, M. A Systematic Study on the Double-Layered Photosensitizing Dye Structure on the Surface of Pt-Cocatalyst-Loaded TiO₂ Nanoparticles. *Bull. Chem. Soc. Jpn.* **2019**, *92*, 1793–1800.

47.   Yoshimura, N.; Kobayashi, A.; Genno, W.; Okubo, T.; Yoshida, M.; Kato, M. Photosensitizing Ruthenium(II)-Dye Multilayers: Photoinduced Charge Separation and Back Electron Transfer Suppression. *Sustain. Energy Fuels* **2020**, *4*, 3450–3457.

48.   Yoshimura, N.; Kobayashi, A.; Yoshida, M.; Kato, M. Enhancement of Photocatalytic Activity for Hydrogen Production by Surface Modification of Pt-TiO₂ Nanoparticles with a Double Layer of Photosensitizers. *Chem. Eur. J.* **2020**, *26*, 16939–16946.

49.   Hanson, K.; Brennaman, M. K.; Ito, A.; Luo, H.; Song, W.; Parker, K. A.; Ghosh, R.; Norris, M. R.; Glasson, C. R. K.; Concepcion, J. J.; Lopez, R.; Meyer, T. J. Structure−Property Relationships in Phosphonate-Derivatized, Ru^{II} Polypyridyl Dyes on Metal Oxide Surfaces in an Aqueous Environment. *J. Phys. Chem. C* **2012**, *116*, 14837–14847.

50.   Ogunsolu, O. O.; Wang, J. C.; Hanson, K. Increasing the Open-Circuit Voltage of Dye-Sensitized Solar Cells via Metal-Ion Coordination. *Inorg. Chem.* **2017**, *56*, 11168–11175.

51.   Kobayashi, A.; Shimizu, K.; Watanabe, A.; Nagao, Y.; Yoshimura, N.; Yoshida, M.; Kato, M. Two-Step Vapochromic Luminescence of Proton-Conductive Coordination Polymers Composed of Ru(II)-Metalloligands and Lanthanide Cations. *Inorg. Chem.* **2019**, *58*, 2413–2421.

52.   Troian-Gautier, L.; Turlington, M. D.; Wehlin, S. A. M.; Maurer, A. B.; Brady, M. D.; Swords, W. B.; Meyer, G. J. Halide Photoredox Chemistry. *Chem. Rev.* **2019**, *119*, 4628–4683.

53.   Troian-Gautier, L.; Swords, W. B.; Meyer, G. J. Iodide Photoredox and Bond Formation Chemistry. *Acc. Chem. Res.* **2019**, *52*, 170–179.

54.   Sasaki, Y.; Kato, H.; Kudo, A. [Co(bpy)₃]$^{3+/2+}$ and [Co(phen)₃]$^{3+/2+}$ Electron Mediators for Overall Water Splitting under Sunlight Irradiation Using Z-Scheme Photocatalyst System. *J. Am. Chem. Soc.* **2013**, *135*, 5441–5449.

55.   Awtrey, A. D.; Connick, R. E. The Absorption Spectra of I₂, I₃⁻, I⁻, IO₃⁻, S₄O₆⁼ and S₂O₃⁼. Heat of the Reaction I₃⁻ = I₂ + I⁻. *J. Am. Chem. Soc.* **1951**, *73*, 1842–1843.

56.   Palmer, D. A.; Ramette, R. W.; Mesmer, R. E. Triiodide Ion Formation Equilibrium and Activity Coefficients in Aqueous Solution. *J. Solution Chem.* **1984**, *13*, 673–683.

57.   Waltz, W. L.; Pearson, R. G. A Pulse Radiolysis Study of Some Cobalt(III) Complexes. Occurrence of Electronically Excited Cobalt(II) Products. *J. Phys. Chem.* **1969**, *73*, 1941-1952.

58.   Furugori, S.; Kobayashi, A.; Watanabe, A.; Yoshida, M.; Kato, M. Impact of Photosensitizing MultiLayered Structure on Ruthenium(II)-Dye-Sensitized TiO₂-Nanoparticle Photocatalysts. *ACS Omega* **2017**, *2*, 3901–3912.

SYNOPSIS TOC